# Mechanism of biomass activation and ammonia modification for nitrogen-doped porous carbon materials

**Kaixu Li [a#], Wei Chen [a#], Haiping Yang [a, *], Yingquan Chen [a, *], Sunwen Xia [a], Mingwei Xia [a], Xin Tu [b], Hanping Chen [a]**

**[a] State Key Laboratory of Coal Combustion, School of Power and Energy Engineering, Huazhong University of Science and Technology, 430074 Wuhan, China**

**[b] Department of Electrical Engineering and Electronics, University of Liverpool, L69 3GJ Liverpool, U.K.**

**E-mail: li_kaixu@hust.edu.cn, chenwei_hk@163.com, yhping2002@163.com, chenyingquan@hust.edu.cn, xiawen@hust.edu.cn, sam_xia@hust.edu.cn, xin.tu@liv.ac.uk, fbghust@163.com.**

# These authors contributed equally to this work.
* Corresponding author.
Tel: +086+027-87542417-8109
E-mail: yhping2002@163.com (H. Yang); chenyingquan@hust.edu.cn (Y. Chen)

**Abstract**

The effect of chemical activation and $NH_3$ modification on activated carbons (ACs) was explored via two contrasting bamboo pyrolysis strategies involving either two steps (activation followed by nitrogen doping in $NH_3$ atmosphere) or one step (activation in $NH_3$ atmosphere) with several chemical activating reagents (KOH, $K_2CO_3$, and KOH+$K_2CO_3$). The ACs produced by the two-step method showed relatively smaller specific surface areas (~90% micropores) and lower nitrogen contents. From the one-step method, the ACs had larger pore diameters with about 90% small mesopores (2 to 3.5 nm). Due to a promotion effect with the KOH+$K_2CO_3$ combination, the AC attained the greatest surface area (2417 $m^2 g^{-1}$) and highest nitrogen content (3.89 wt.%), endowing the highest capacitance (175 F $g^{-1}$). The balance between surface area and nitrogen content recommends KOH+$K_2CO_3$ activation via the one-step method as the best choice for achieving both greener production process and better pore structure.

**Keywords:** Biomass activation; $NH_3$ modification; Nitrogen-doped; Porosity; Supercapacitors

## 1. Introduction

Due to their easy preparation and porous structures with large surface areas, activated carbons (ACs) have been used in many scientific applications in which large adsorption areas are needed. When combined with biomass pyrolytic polygeneration, AC production becomes an environmentally friendly and low-cost technology (Yang et al., 2016). ACs have been widely used as electrode materials for energy storage (Frackowiak and Béguin, 2001), sorbents for gas separation/storage (Choi et al., 2009) and water purification (Li et al., 2017), additives for soil amendment (Tan et al., 2017), and supports for many important catalytic processes (Borghei et al., 2017). However, for all these applications, the mass diffusion and adsorption of, for example, electrolyte ions or gas molecules on the AC surface are processes of fundamental importance (Salanne et al., 2016), and certain reactions such as hydrolysis and oxygen reduction require active sites (Lee et al., 2017). Thus, the performance of these applications is highly contingent on the accessibility of adsorption and active sites dispersed throughout the internal and external surfaces of the ACs.

To prepare high-quality AC materials, two main aspects must be considered (Bhatnagar et al., 2013): chemical activation, to tailor the micro- and mesopore structure with a high specific surface area; and the generation of active sites by the substitutional doping of heteroatoms such as nitrogen (Paraknowitsch and Thomas, 2013), sulfur (Gu et al., 2013), boron (Shcherban et al., 2017), and phosphorus (Denisa et al., 2009) into the carbon lattice. To optimize the microstructure, chemical activating agents such as KOH, $ZnCl_2$, $Na_2CO_3$, $K_2CO_3$, $NaHCO_3$, NaOH, and $H_3PO_4$

are often used (Kula et al., 2008; Li et al., 2015; Oliveira et al., 2018; Tian et al., 2018). Among these, KOH is most frequently reported in the literature, because ACs activated by KOH possess well-defined micropore size distributions and ultrahigh specific surface areas (Lv et al., 2012). $K_2CO_3$, a frequently used food additive, is an environmentally friendly activator that can mitigate the corrosion of equipment at high temperatures compared to KOH. In addition, mixed activators have attracted attention by combining different activation effects. Li et al. (Li et al., 2015) obtained AC materials with perfect hierarchical pore structures by mixed activation. In that case, the use of KOH added new micropores by corrosion of the carbon surface, while the decomposition of $K_2CO_3$ enlarged the pore sizes at a certain temperature. To improve surface characteristics, the most important and widely introduced heteroatom is nitrogen, and nitrogen-containing functional groups can enhance the interactions between the AC surface and acidic molecules (Shen and Fan, 2013), which is beneficial for the oxygen reduction reaction (Guo et al., 2016), pseudocapacitance (Lota et al., 2005), catalysis (Shen et al., 2014), and so on. Among the common nitrogen sources (e.g., $NH_3$, HCN, urea, melamine, and polyaniline), ammonia has been the most frequently used reagent for introducing nitrogen into porous carbons (Shen and Fan, 2013).

Numerous routes have been developed to synthesize N-doped porous carbons via a combination of the two aspects mentioned above (Liu et al., 2018), and include three different strategies: (1) a two-step method based on nitrogen functionalization followed by chemical activation; (2) a two-step method involving chemical activation

followed by nitrogen functionalization; and (3) a one-step method entailing direct pyrolysis of the mixture of biomass, nitrogen source, and chemical activator. For method (1), according to our previous study, the activation step destroys the nitrogen-containing groups by an etching action (W. Chen et al., 2018b); therefore, this approach is not a good choice for increasing the amount of nitrogen. For method (2), the activation step can create a porous structure which allows $NH_3$ to enter deep into the pore structure, thus facilitating uniform nitrogen doping. However, ammonia molecules (and ammonia free radicals) preferentially react with surface oxygen-containing functional groups, and hence, additional mild surface oxidation is usually needed (Laheaar et al., 2014). There seems to be a competition between optimizing the microstructure and improving surface characteristics. Moreover, for the one-step strategy (method (3)), compared with the two-step methods, interactions between the chemical activation and $NH_3$ modification processes may exert as-yet unknown effects. Luo et al. (Luo et al., 2014) presented a simple one-step fabrication method for nitrogen-doped nanoporous carbon membranes by annealing cellulose filter paper under $NH_3$. They found that the reaction between the N-doped carbon and $NH_3$ leads to carbon gasification, resulting in a large surface area (up to 1973.3 $m^2 g^{-1}$). This result indicates that $NH_3$ modification has some interesting effects in tailoring pore structure. Chen et al. (Chen et al., 2016) investigated the influence of the addition of $NH_3$ and KOH on the fast pyrolysis of bamboo, and found that the amount of nitrogen dramatically increased to 10.4 wt% after the addition of KOH, indicating that there is a strong interaction effect for the combination of chemical activation and

$NH_3$ modification. According to results of previous studies, some interactions do happen between the chemical activation and the $NH_3$ modification，but how the interaction happened, it is still unknown, furthermore, most researches are based on separated stages, like get char first, then activated with KOH or $K_2CO_3$, followed with N-doping with ammonia. As we known, there are few O-compound and not easy for activation and doping. Combined the three steps into one might be a good choice. Therefore, it would be interesting to further investigate these two aspects: first, chemical activation under $NH_3$ atmosphere, for which the mechanisms of pore tailoring and nitrogen doping are yet unknown; and second, the different interaction effects that occur due to the use of various activating reagents.

To analyze the interaction effects between chemical activation and $NH_3$ modification on the properties of ACs, the two processes were combined in either a two-step method (chemical activation followed by nitrogen doping in an $NH_3$ atmosphere) or a one-step method (chemical activation in an $NH_3$ atmosphere), with KOH and $K_2CO_3$ as the chemical activating reagents. A mixed activator (KOH+$K_2CO_3$) was also studied to investigate any possible synergy, and simultaneously achieve greener production process and improved AC structure. The most essential factors affecting the performance of ACs (porous structure, N-doping concentrations and types) were the focal points of our investigation. Furthermore, the mechanisms of pore tailoring and nitrogen doping during the combined chemical activation/$NH_3$ modification were studied in depth. Finally, to elucidate potential advantages for applications as supercapacitor electrodes, the electrochemical behavior

of all the ACs was measured, especially that material with the highest specific capacitance. The results we present provide valuable insights that should aid in the development of porous carbon materials with improved properties.

## 2. Materials and methods

### 2.1 *Materials*

Bamboo waste was obtained locally. The material was crushed and sieved to achieve a particle size of < 425 μm, and then dried at 105 °C overnight before use. The bamboo waste consisted of large volatile (80.57 wt%) and small ash (2.32 wt%) components, with carbon (41.97 wt%) and oxygen (43.18 wt%) as the main elements and negligible nitrogen content (0.27 wt%) (Chen et al., 2017). Activation chemicals KOH (≥ 85%) and $K_2CO_3$ (≥ 99%), both analytical reagent grade, were obtained from Sinopharm Chemical Reagent Co., Ltd.

Bamboo waste was initially impregnated with the chemical activation reagent (chemical reagent/bamboo weight ratio 2:5) (Chen et al., 2016), using KOH, $K_2CO_3$, or a combination of KOH+$K_2CO_3$ (1:1 w/w). The mixture was stirred at 60 °C overnight until it was completely dry.

### 2.2 *Experimental methods*

Slow pyrolysis was performed in a fixed-bed system that consisted of a fixed-bed reactor (height, 1000 mm; diameter, 35 mm), electronic-control furnace, gas-flow controller, temperature controller, ice-water condensing unit, gas cleaner, and drying unit. (E-supplementary data of this work can be found in online version of the paper)

For the two-step method, the dried, impregnated material was inserted into the fixed-bed system under a continuous flow of Ar (200 mL/min) for the entire process. When the system reached a steady state (no air in the reactor, about 30 min), the material was heated to 800 °C at a rate of 20 °C/min, maintained for 1 h, and then cooled to ambient temperature under Ar purging. To remove the potassium-containing compounds, the resultant grains were first immersed in a dilute solution of HCl, and then washed with abundant distilled water until pH ≈ 7 was obtained. After drying overnight at ~80 °C, the washed product was heated under a flow of $NH_3$ (200 mL/min) to 800 °C (at a rate of 20 °C/min), maintained for 1 h in the pyrolysis reactor, and then cooled to ambient temperature under Ar purging. The end products are designated as *T*-*x*, where *x* is the chemical activation reagent; the sample obtained without the addition of a chemical reagent is named *T*-AC.

For the one-step method, the dried, impregnated material was carbonized under a flow of $NH_3$ (200 mL/min) at 800 °C (20 °C/min, 1 h), following the same procedure for the first step of the two-step method. Then, the washed product was dried overnight at around 80 °C. These samples are designated as *O*-*x*, where *x* is the chemical activation reagent; the sample obtained without the addition of a chemical reagent attained is named *O*-AC.

2.3 *Characterization*

The porous characteristics of our ACs were measured using nitrogen isothermal adsorption-desorption at 77 K with an accelerated surface area and porosimetry system (ASAP 3000, Micromeritics, USA). Prior to adsorption, the samples were

degassed at 150 °C for 10 h. The Brunauer-Emmett-Teller (BET) specific surface area ($S_{BET}$) was determined using the BET equation. The micropore surface area ($S_{mic}$) and micropore volume ($V_{mic}$) were determined by the *t*-plot method. The total pore volume ($V_{total}$) was determined by single-point adsorption total pore volume analysis. The average pore diameter ($D$) was obtained as $4V/S_{BET}$, based on the BET method. The pore size distribution plot was obtained by the Barrett–Joyner–Halenda (BJH) method. The morphology of the ACs was measured using field emission scanning electron microscopy (FESEM; Sirion 200, FEI, Netherlands), operating at 10 kV.

The crystal structure of the ACs was examined by X-ray diffraction (XRD; X'Pert PRO, PANalytical B.V., Netherlands), using a scanning step of 0.026° in the 2θ range from 10° to 90°. To determine the graphitic quality, Raman scattering spectra of the ACs were collected on a LabRAM HR800 (Horiba Jobin Yvon, Japan) over the range of Raman shifts from 500 to 3500 $cm^{-1}$.

Ultimate analysis of the samples was conducted using a CHNS/O elementary analyzer (Vario Micro Cube, Germany). The nitrogen-containing functional groups on the surface of the ACs were analyzed by X-ray photoelectron spectroscopy (XPS, Axis Ultra DLD, Kratos, UK) using the Al Kα line (15 kV, 10 mA, 150 W) as the radiation source. The C 1*s* peak position at 285 eV was used as an internal standard. The curves of the N 1*s* peaks were fitted by the XPS Peak 4.1 software. The content of each element was determined from the corresponding peak area and calibrated by the atomic sensitivity factor with C as reference.

2.4 *Electrochemical measurements*

The electrochemical performance of the ACs was measured in 6 M KOH using a three-electrode system (CH Instruments 760, USA) at room temperature. A platinum plate and saturated calomel electrode were used as the counter and reference electrodes, respectively. The working electrode was prepared by uniformly mixing the AC (80 wt%) with acetylene black (10 wt%) and poly(vinylidene fluoride) (PVDF, 10 wt%) in *N*-methyl-2-pyrrolidone (NMP) to form a homogeneous slurry. The slurry was coated onto a 1 cm × 1 cm nickel foam current collector and dried at 105 °C for 12 h in a vacuum oven. Finally, it was pressed at 10 MPa, and the mass difference was obtained to calculate the AC mass on the working electrode.

## 3. Results and discussion

3.1 *Pore characteristics and morphology analysis*

The $N_2$ sorption isotherms and pore size distributions of the prepared samples are shown in Figure 1. All the ACs produced by the two-step method have type I(a) isotherms with significant nitrogen adsorption amount at relative pressures $p/p_0 < 0.1$, and no obvious hysteresis loop at high relative pressures $p/p_0 > 0.4$ (Figure 1(a), inset); this behavior is typical of mainly narrow microporous materials. By contrast, all the ACs prepared by the one-step method show type I(b) isotherms in which the $N_2$ uptake capacity increases prominently at low relative pressure ($p/p_0$ = 0.1–0.3, Figure 1(b), inset), as is typical of wide microporous, and possibly narrow mesoporous, materials (Thommes et al., 2015). As expected, *O*-KOH and *O*-KOH+$K_2CO_3$

absorbed larger volumes of nitrogen (about 400 $cm^3\ g^{-1}$) than the other samples, which suggests their greater specific surface areas; their pore size distributions (Figure 1, main plots) are consistent with this analysis. Furthermore, the existence of some medium-sized mesopores (5 to 15 nm) in *T*-KOH can be proven by the small conspicuous hysteresis loop with a high relative pressure range ($p/p_0$ = 0.45–1.0). Finally, *O*-KOH, *O*-$K_2CO_3$, and *O*-KOH+$K_2CO_3$ contain a larger volume of small mesopores (2 to 3.5 nm), matching the "knees" in their $N_2$ sorption isotherms.

Detailed structural parameters of the porous carbons were calculated from the $N_2$ adsorption isotherms and are summarized in Table 1. The porosity of the AC materials is significantly influenced by the choice of activator and method. With the addition of the activators, all the ACs had greater specific surface areas and total pore volumes. The $S_{BET}$ values of *T*-KOH and *T*-$K_2CO_3$ increased to ~1270 $m^2\ g^{-1}$, while that of *T*-KOH+$K_2CO_3$ was slightly lower at only 1123 $m^2\ g^{-1}$, demonstrating the inhibition effect on surface area development when combining KOH and $K_2CO_3$. The *O*-KOH sample exhibited the largest surface area (up to 2892 $m^2\ g^{-1}$) among the ACs, while *O*-$K_2CO_3$ and *T*-$K_2CO_3$ had similar surface areas. *O*-KOH+$K_2CO_3$ had a larger surface area (2417 $m^2\ g^{-1}$) than *T*-KOH+$K_2CO_3$, and was also significantly higher than the equivalent average value for *O*-KOH and *O*-$K_2CO_3$; this result demonstrates the promotion of surface area development when combining KOH and $K_2CO_3$. The changes in the total pore volume trend are the same as those for $S_{BET}$.

All the ACs produced by the two-step method were observed to have 78–86% of their surface area as micropores, because the lower chemical reagent/bamboo weight

ratio (2:5) promoted a microporous structure (Hou et al., 2014); whereas, all the ACs produced by the one-step method only showed 2–9% for this metric, and small mesopores instead formed the principal component of their pore structure. As described above, it is obvious that *O*-KOH, *O*-$K_2CO_3$, and *O*-KOH+$K_2CO_3$ produced larger numbers of pores with larger diameters than did *T*-KOH, *T*-$K_2CO_3$, and *T*-KOH+$K_2CO_3$, which is consistent with the changing trend of average pore diameter. Among these, *T*-KOH had an abnormal average pore diameter due to the existence of medium-sized mesopores (5 to 15 nm).

To understand the inhibition and promotion effects on surface area development when combining KOH and $K_2CO_3$ as the activator, the differences between the KOH and $K_2CO_3$ activation mechanisms must be elucidated. Both KOH and $K_2CO_3$ tailor the porous structure through carbon oxidation and hydroxide reduction (Wang and Kaskel, 2012). The activation process can be described as follows. At temperatures in the range of 475–570 °C, microporosity develops due to the corrosion of the carbon surface by KOH, as shown in reaction (1) below. At higher temperatures, up to 700 °C, the decomposition of $K_2CO_3$ enlarges the pore size, with the release of CO and $CO_2$ and formation of metallic K, as shown in reactions (2)–(4).

$$6KOH + 2C \rightarrow 2K + 3H_2 + 2K_2CO_3 \quad (1)$$

$$K_2CO_3 + 2C \rightarrow 2K + 3CO \quad (2)$$

$$K_2CO_3 \rightarrow K_2O + CO_2 \quad (3)$$

$$K_2O + C \rightarrow 2K + CO \quad (4)$$

When present, $NH_3$ starts to decompose during the heating process near 500 °C (E.

P. Perman and G. A. S. Atkinson, 1904), resulting in various free radicals that attack the carbon active sites present on the AC surface. Due to its weak etching capacity, $NH_3$ can slightly increase the micropore volume via the following possible pathway (Chen et al., 2016; Luo et al., 2014), which contributes to a bigger surface area of *O*-AC than *T*-AC:

$$(C)_{bamboo} + NH_3 \rightarrow C^* + H^* + NH^* + NH_2^* \rightarrow H_2 + C-NH + C-NH_2 \quad (5)$$

During the first stage (around 500 °C) of the slow pyrolysis to form *T*-KOH, alteration of the molecular chain structures results in the increment of multiple fused benzene rings and a sharp decrease of methylene and oxygen-containing functional groups (Huang et al., 2015). Therefore, under these conditions, the semi-char is believed to be in a "non-activating" state in which it is not easy to be etched further during the second stage with very limited active sites on its surface (Elmouwahidi et al., 2017). As the etching action of KOH destroyed many oxygen-containing functional groups on the surface of semi-char which is surrounded by inert atmosphere, exposing many defect sites without active substances to bind with; this is called the "non-activating carbon". Then, in the second stage (up to 700 °C), an enlargement of the pore size commences via reactions (2)–(4), on the basis of reaction (1), leading to a quite large surface area. In the first stage of *T*-$K_2CO_3$ synthesis, many oxygen-containing functional groups in the semi-char are retained, so that a low-level "activating" state is preserved, without the KOH etching reaction. Then, the violent etching action of $K_2CO_3$ results in a surface area that is quite large. However, for *T*-KOH+$K_2CO_3$, the KOH etching reaction leads to the "non-activating carbon" state.

Comparing the second stage of *T*-$K_2CO_3$ and *T*-KOH+$K_2CO_3$, the impregnated $K_2CO_3$ in *T*-$K_2CO_3$ etched the low-level "activating" semi-char, but the impregnated $K_2CO_3$ in *T*-KOH+$K_2CO_3$ etched the "non-activating" semi-char, leaving less site for $K_2CO_3$ etching than in the case of *T*-$K_2CO_3$. Thus, an inhibition effect occurs: the surface area of the *T*-KOH+$K_2CO_3$ sample is reduced with respect to that of either the *T*-KOH or *T*-$K_2CO_3$ sample.

For the one-step method, the reaction process is the same as that of the two-step method, except that it occurs under $NH_3$ atmosphere (Figure 2). For *O*-KOH, when the temperature reaches ~500 °C, reaction (1) begins to play a major role in the etching decomposition of the bamboo. The methylene and ether bridges linking the high molecular weight compounds break to form gas fuel, bio-oil, and semi-char. However, considering the highly active atmosphere, $NH_3$ and its free radicals ($NH_2$*, NH*, and H*) become heavily involved, introducing many nitrogen-containing functional groups to the semi-char surface. Therefore, it can be inferred that the semi-char is placed in an "activating" state in which it is easy to be etched further with many active sites on its surface, since $NH_3$ has been involved into the etching action of KOH, introducing many nitrogen-containing functional groups to the semi-char surface by $NH_3$ binding with those defect sites. And it may therefore be designated an "activating carbon" under these conditions. When the temperature reaches 700 °C, reactions (2)–(4) begin to play a greater role in expanding the pore structure. Due to the high reactivity of this "activating carbon," a violent etching action results in the highest value of $S_{BET}$. For *O*-$K_2CO_3$, when the temperature

reaches ~500 °C, due to the weight loss via the bamboo pyrolysis that occurs mainly between 300 and 550 °C (Zhu et al., 2008), the semi-char still includes some nitrogen-containing functional groups but also attains a relatively low-level "activating" state due to the lack of etching reaction (1). Thus, the surface area of the AC treated with $K_2CO_3$ is lower than that of *O*-KOH. In theory, the degree of the "activating" state obtained is similar to that of *O*-$K_2CO_3$, which is supported by the fact that we observe similar $S_{BET}$ values for *T*-$K_2CO_3$ and *O*-$K_2CO_3$. Interestingly, for *O*-KOH+$K_2CO_3$, the presence of KOH meant that the semi-char reached the "activating" state during the first stage, and then $K_2CO_3$ (including the original impregnant material as well as the product of reaction (1)) expanded the pore structure during the second stage. It is worth mentioning that during the second stage of the generation of *O*-KOH+$K_2CO_3$, the impregnated $K_2CO_3$ has more scope for etching than it does during *O*-$K_2CO_3$ generation. Thus, promotion effect occurs which results in a greater surface area for the *O*-KOH+$K_2CO_3$ sample than the average of the AC surface areas produced by the individual KOH and $K_2CO_3$ activators.

In addition, larger pore diameters result from the strong interaction effect between chemical activation and $NH_3$ modification in the one-step method. Chemical activation creates many oxygen-containing functional groups at the pores by the etching decomposition of the bamboo, while $NH_3$ and its free radicals ($NH_2$*, NH*, and H*) react with them to increase pore diameters, form new pores, and increase the number of nitrogen-containing functional groups (Zhang et al., 2016). This effect is another factor that contributes to the larger surface areas and total pore volumes in

samples produced by the one-step method.

The ACs produced by the two-step method show similar morphologies to those produced by the one-step method with the corresponding activators (E-supplementary data of this work can be found in online version of the paper). The microscopic morphology of *O*-AC is characterized by a smooth surface and multiple highly ordered empty spaces (of several microns in size) which could be mainly attributed to the inherent structure of the biomass material (Ray et al., 2004). With KOH, $K_2CO_3$, and KOH+$K_2CO_3$ activation, the surface becomes uneven and many randomly arranged holes (hundreds of nanometers) are observed, due to the thinning or breaking of the barriers between the empty spaces. The interconnected hole structure not only provides good bearing surfaces for mesopores and micropores, but also facilitates rapid mass diffusion, buffering, and storage, thus promoting the utilization of the porous networks (Presser et al., 2011). In conclusion, in our experiment, activation by the potassium compounds had the strongest effect on the microscopic morphology of the ACs, and this process may even have the power to destroy the initial structure of the bamboo. In contrast, we observed that $NH_3$ modification played a much lesser role in the modification of the microscopic structure.

3.2 *Chemical structure*

All the ACs produced by potassium-compound activation, whether via the one- or two-step method, display low-intensity peaks (E-supplementary data of this work can be found in online version of the paper), suggesting relatively low graphitic crystallinity, with their graphitic architecture severely disrupted through chemical

activation (Chen et al., 2018). No obvious difference is seen between the one-step and two-step methods, indicating that there might be no obvious interaction effect on the crystallographic structure of the ACs.

The Raman spectra further confirm the graphitic structure through the peak-height ratio of the *D* and *G* peaks, which is denoted as $I_D/I_G$. A higher value of $I_D/I_G$ indicates a lower graphitization degree. Due to the overlap of the *D* and *G* bands, peak fitting was performed, following the procedure outlined by Vallerot (Vallerot et al., 2006). All the samples show features that are similar to those of the main peaks of graphitic materials, with *D* and *G* bands at ~1335 and ~1587 $cm^{-1}$, respectively. The value of $I_D/I_G$ is increased for the samples that underwent chemical activation, indicating a reduction in the degree of graphitization. This implies that activation results in the generation of many defects, i.e., a structural disorder reflected in the intensity of the Raman *D* band. Furthermore, similar inhibition and promotion effects can be seen by comparing the values of $I_D/I_G$ for KOH, $K_2CO_3$, and KOH+$K_2CO_3$. However, the detailed mechanism is still unclear and will need to be investigated in the future. The values of $I_D/I_G$ for the ACs produced by the two-step method are slightly higher than those of the one-step method corresponding to the same activators; this phenomenon may be related to the pair of heat-treatment steps of the two-step method (Huang et al., 2013).

3.3 *N-doping concentrations and types*

Treatment of bamboo with $NH_3$ introduces an appreciable amount of nitrogen into the AC matrix (Table 2). For the two-step method, the use of KOH results in a lower

nitrogen content (1.15 wt%) than that of *T*-AC (1.68 wt%), but using $K_2CO_3$ produces a higher content (2.64 wt%). With KOH+$K_2CO_3$ activation, however, only 1.08 wt% nitrogen was measured in the resulting AC, which is obviously much lower than the amounts measured in *T*-KOH and *T*-$K_2CO_3$, indicating the inhibition effect on nitrogen doping when combining KOH and $K_2CO_3$. For the one-step method, *O*-KOH (2.27 wt%) had a lower nitrogen content than *O*-AC (2.99 wt%), and a higher nitrogen content was measured for *O*-$K_2CO_3$ (3.17 wt%). The *O*-KOH+$K_2CO_3$ sample had the highest nitrogen content (3.89 wt%), indicating the clearly promotion of nitrogen doping when combining KOH and $K_2CO_3$.

For all the AC samples generated with the same activator, the amount of nitrogen detected in the sample produced by the one-step method is higher than in that produced by the two-step method, indicating that the former is more effective for nitrogen doping. This is because, in the one-step method, chemical activation by attack of the bamboo creates many active substances with which $NH_3$ can react to form nitrogen-containing functional groups. This mechanism is consistent with the interaction effect on increasing pore diameter. By contrast, during the first step of the two-step method, the active substances are removed.

The mechanism of the promotion and inhibition effects on nitrogen doping is the same as the effect on surface area. For the two-step method, KOH etching (reaction (1)) destroys many oxygen-containing functional groups, leaving a “non-activating carbon” in the inert atmosphere. Thus, the amount of nitrogen in the *T*-KOH sample is lower than that in *T*-AC. Further, the etching ability of $K_2CO_3$ is obviously lower than

that of KOH, leaving more active substances in the resultant AC at the end of the first step. Thus, the amount of nitrogen measured in the *T*-$K_2CO_3$ sample is higher than that produced by KOH activation. When combining KOH and $K_2CO_3$, on the one hand, KOH still produces the "non-activating carbon", accompanied by a sharp decrease of oxygen-containing functional groups; on the other hand, the impregnated $K_2CO_3$ consumes the active substances. Thus, an inhibition effect occurs, such that the amount of nitrogen in the AC produced by KOH+$K_2CO_3$ activation is slightly lower than that produced by the use of either KOH or $K_2CO_3$ as the activator.

For the one-step method, it is worth mentioning that $NH_3$ modification also has a competitive relationship with chemical activation because the activation process can destroy active substances, including nitrogen-containing functional groups, but nitrogen doping is achieved mainly by the reaction of $NH_3$ with active substances (those containing C=O or –OH, Eqs. (6) and (7)) (W. Chen et al., 2018a). For *O*-KOH, etching reaction (1) results in the "activating carbon" at the cost of many oxygen-containing functional groups, due to excessive corrosion. This is not conducive to nitrogen doping during the second stage when $K_2CO_3$ destroys many of the nitrogen-containing functional groups. However, for *O*-$K_2CO_3$, etching reactions (2)–(4) improve the amount of nitrogen doping by the abovementioned interaction effect. When combining KOH and $K_2CO_3$, a good balance is achieved between the degree of the obtained "activating" state and the number of oxygen-containing functional groups. Thus, the amount of nitrogen in *O*-KOH is lower than that in *O*-AC, and the amount of nitrogen in *O*-$K_2CO_3$ is almost equal to that in *O*-AC. However, the

amount of nitrogen in *O*-KOH+$K_2CO_3$ is higher than the average of that in *O*-KOH and *O*-$K_2CO_3$.

$$NH_3/NH_2^*/NH^* + (-C=O) \rightarrow -CO-NH_2 \quad (6)$$

$$NH_3/NH_2^*/NH^* + (-C-OH) \rightarrow (-C-NH_2) + H_2O \quad (7)$$

XPS measurements and ultimate analysis were employed to study the surface functionalities and compositions of the ACs. The nitrogen content in the ACs produced by the two-step method, as measured by ultimate analysis (*T*-$N_{UA}$), is higher than that measured by XPS (*T*-$N_{XPS}$) for all activators, while equivalent values for the one-step method, *O*-$N_{UA}$ and *O*-$N_{XPS}$, are quite similar. These results indicate a distribution of *T*-$N_{UA}$ mainly localized on the surface of the micropore channels due to $NH_3$ and its free radicals ($NH_2$*, NH*, and H*) having greater capacity to enter deep into the micropores. Moreover, the distribution of *O*-$N_{UA}$ and *O*-$N_{XPS}$ values indicates that there are no differences between the external surfaces and the surfaces of small mesopore channels. Due to the etching decomposition of the bamboo, volatile compounds was thoroughly exposed to $NH_3$ atmosphere, leaving the uniform distribution of nitrogen.

The N 1*s* spectra can be deconvoluted into four peaks, specifically pyridinic-N (398.5 ± 0.3 eV), pyrrolic-N (400.5 ± 0.3 eV), quaternary-N (401.2 ± 0.3 eV), and oxidized-N (403.2 ± 0.3 eV) (Hulicova-Jurcakova et al., 2009b; Sun et al., 2014; Xu et al., 2012). Typical XPS spectra for the nitrogen-doped ACs are provided in Figure 3. With the addition of the K compounds, irrespective of method, the area proportions of pyridinic-N and pyrrolic-N in the spectra increase, while the quaternary-N area

proportions decrease sharply. For the two-step method, both for *T*-KOH and *T*-$K_2CO_3$, pyridinic-N attains the greatest percentage (about 38%). However, when combining the KOH and $K_2CO_3$ activators, the amounts of pyridinic-N and pyrrolic-N in the end products are similar (about 33%), and the total amount of pyridinic-N and pyrrolic-N does not change with respect to those of *T*-KOH or *T*-$K_2CO_3$ (about 65%). For the one-step method, with KOH addition, pyridinic-N dominates (up to 42.08%), while pyrrolic-N is the main species when $K_2CO_3$ is added (up to 51.64% ), and the total amount of pyridinic-N and pyrrolic-N is similar (about 75%). When KOH and $K_2CO_3$ are used in combination, the main N species are pyridinic-N and pyrrolic-N (up to 30% for each), and their total amount drops to about 65%. It is well-known that pyridinic-N and pyrrolic-N are especially beneficial in enhancing the performance of an AC material, for example, by generating pseudo-capacitive behaviour in supercapacitor applications (Cordero-Lanzac et al., 2018) and providing oxygen reduction sites (Guo et al., 2016). These functional groups might result from $NH_3$ reacting with oxygen-containing groups (Eqs. (6) and (7)), while the more stable quaternary-N might result from transformation of pyridinic-N through rearrangement of carbon and nitrogen atoms (Lin et al., 2012; Zhao et al., 2015).

3.4 *Electrochemical behavior*

To qualitatively evaluate the electrochemical performance of these AC electrode materials, cyclic voltammetry (CV), galvanostatic charge–discharge (GCD), and electrochemical impedance spectroscopy (EIS) were carried out in a three-electrode system using 6 M KOH aqueous electrolyte (E-supplementary data of this work can

be found in online version of the paper).

The CV curves of the AC electrode materials at a scan rate of 10 mV $s^{-1}$, show not only nearly rectangular shapes but also some peaks, especially for the nitrogen-doped ACs produced by the one-step method. This indicates that the increased CV curve area is the result of both the electric double-layer capacitance of the AC and the faradic pseudo-capacitance of nitrogen in the AC lattice.

The GCD curves of the AC electrode materials at a charge–discharge current density of 1.0 A $g^{-1}$ with a potential window from −0.9 to 0.1 V. Clearly, due to the greater specific surface areas and the higher nitrogen content, the ACs produced by One-step method show the higher specific capacitances and the more obvious pseudo-capacitance peak respectively. And *O*-KOH+$K_2CO_3$ presents the best supercapacitive performance among them, with a specific capacitance as high as 175 F $g^{-1}$ at 1.0 A $g^{-1}$. This may be due to the greater surface area (2417 $m^2$ $g^{-1}$) and highest nitrogen content (3.89 wt.%). In particular, *T*-KOH and *O*-$K_2CO_3$ have greatly different nitrogen content (1.15 wt.% and 3.17 wt.%, respectively) and similar specific areas (about 1260 $m^2$ $g^{-1}$), but similar specific capacitance (108 F $g^{-1}$). This may be due to pore-size differences where *T*-KOH mainly consists of micropores but *T*-$K_2CO_3$ is small mesopores. And certain pore-size micropore (less than 1nm) is beneficial to double-layer capacitance (Chmiola et al., 2006). The curves of the nitrogen-doped electrode materials deviate slightly from linearity, which is probably due to the presence of a pseudo-capacitance effect of the quick redox reaction.

The CV curves (Figure 4(a)) of the *O*-KOH+$K_2CO_3$ electrode at different voltage

sweep rates display similar rectangular shapes but no obvious peaks are observed, even at a scan rate of 100 mV $s^{-1}$, which is attributed to the lower inner resistance and hysteresis effect of the redox reaction of the nitrogen heteroatoms, respectively. In addition, the porous structure also facilitates the diffusion of electrolyte ions, thus improving the electrochemical performance. The GCD curves of the *O*-KOH+$K_2CO_3$ electrode at different current densities are displayed in Figure 4(b) (inset). The mild decrease in specific capacitance with the increase in current density, shown in Figure 4(b), occurs because the slower redox reaction of the nitrogen heteroatoms and faster diffusion of electrolyte ions cannot keep pace with the increased current density. From Figure 4(b), it can also be observed that, at a current density of 1 A $g^{-1}$, the capacitance reaches 175 F $g^{-1}$. After increasing the current density to 20 A $g^{-1}$, the capacitance decreases to 100 F $g^{-1}$, retaining ~57.1% of the initial value, suggesting that *O*-KOH+$K_2CO_3$ has a high rate performance. Comparing with the results of literature (González-García, 2018; Wang et al., 2017), its specific capacitance is at medium level, but the great surface area is really competitive. In short, the *O*-KOH+$K_2CO_3$ electrode material demonstrates good capacitive behavior due to its competitive porous structure and relatively higher nitrogen content (up to 3.89 at%).

## 4. Conclusion

For the one-step method, larger pore diameters and higher doped-nitrogen contents result from the interaction effect where $NH_3$ and its free radicals react with oxygen-containing functional groups at the pores by chemical etching that induces the

decomposition of the bamboo. When combining KOH and $K_2CO_3$, a good balance between the degree of the "activating" state and the number of oxygen-containing functional groups, causes a significantly larger $S_{BET}$ (2417 $m^2 g^{-1}$) and the highest $N_{UA}$ (3.89 wt%). The promoting effect recommends the one-step method with the KOH+$K_2CO_3$ as the best choice for simultaneously achieving greener production process and better pore structure.

**Acknowledgements**

We express great appreciation for financial support from the National Nature Science Foundation of China (51876078, 51622604 and 51861130362), the Foundation of the State Key Laboratory of Coal Combustion (FSKLCCA1805), and the China Postdoctoral Science Foundation (2018M640696), as well as technical support from the Analytical and Testing Center at the Huazhong University of Science & Technology (http://atc.hust.edu.cn).

## References


1. Bhatnagar, A., Hogland, W., Marques, M., Sillanpää, M., 2013. An overview of the modification methods of activated carbon for its water treatment applications. Chemical Engineering Journal 219, 499–511. https://doi.org/10.1016/j.cej.2012.12.038
2. Borghei, M., Lehtonen, J., Liu, L., Rojas, O.J., 2017. Advanced Biomass-Derived Electrocatalysts for the Oxygen Reduction Reaction. Advanced Materials 1703691, 1703691. https://doi.org/10.1002/adma.201703691
3. Chen, J., Wei, H., Fu, N., Chen, H., Lan, G., Lin, H., Han, S., 2018. Facile synthesis of nitrogen-containing porous carbon as electrode materials for superior-performance electrical double-layer capacitors. Journal of Materials Science 53, 2137–2148. https://doi.org/10.1007/s10853-017-1664-7
4. Chen, W., Chen, Y., Yang, H., Li, K., Chen, X., Chen, H., 2018a. Investigation on biomass nitrogen-enriched pyrolysis: Influence of temperature. Bioresource Technology 249, 247–253. https://doi.org/10.1016/j.biortech.2017.10.022
5. Chen, W., Chen, Y., Yang, H., Xia, M., Li, K., Chen, X., Chen, H., 2017. Co-pyrolysis of lignocellulosic biomass and microalgae: Products characteristics and interaction effect. Bioresource Technology 245, 860–868. https://doi.org/10.1016/j.biortech.2017.09.022
6. Chen, W., Li, K., Xia, M., Chen, Y., Yang, H., Chen, Z., Chen, X., Chen, H., 2018b. Influence of $NH_3$ concentration on biomass nitrogen-enriched pyrolysis. Bioresource Technology 263, 350–357. https://doi.org/10.1016/j.biortech.2018.05.025
7. Chen, W., Yang, H., Chen, Y., Chen, X., Fang, Y., Chen, H., 2016. Biomass pyrolysis for nitrogen-containing liquid chemicals and nitrogen-doped carbon materials. Journal of Analytical and Applied Pyrolysis 120, 186–193. https://doi.org/10.1016/j.jaap.2016.05.004
8. Chmiola, J., Yushin, G., Gogotsi, Y., Portet, C., Simon, P., Taberna, P.L., 2006. Anomalous Increase in Carbon Capacitance at Pore Sizes Less Than 1 Nanometer. Science 313, 1760–1763.
9. Choi, S., Drese, J.H., Jones, C.W., 2009. Adsorbent materials for carbon dioxide capture from large anthropogenic point sources. ChemSusChem 2, 796–854. https://doi.org/10.1002/cssc.200900036
10. Cordero-Lanzac, T., Rosas, J.M., García-Mateos, F.J., Ternero-Hidalgo, J.J., Palomo, J., Rodríguez-Mirasol, J., Cordero, T., 2018. Role of different nitrogen functionalities on the electrochemical performance of activated carbons. Carbon 126, 65–76. https://doi.org/10.1016/j.carbon.2017.09.092
11. Denisa, H.J., Puziy, A.M., Poddubnaya, O.I., Fabian, S.G., Tascón, J.M.D., Lu, G.Q., 2009. Highly stable performance of supercapacitors from phosphorus-enriched carbons. Journal of the American Chemical Society 131, 5026–5027. https://doi.org/10.1021/ja809265m
12. E. P. Perman and G. A. S. Atkinson, 1904. The Decomposition of Ammonia by heat. Proceedings of the Royal Society of London 110–117. https://doi.org/10.1039/CT9222100698
13. Elmouwahidi, A., Bailón-García, E., Pérez-Cadenas, A.F., Maldonado-Hódar, F.J., Carrasco-Marín, F., 2017. Activated carbons from KOH and $H_3PO_4$-activation of olive residues and its application as supercapacitor electrodes. Electrochimica Acta 229, 219–228. https://doi.org/http://dx.doi.org/10.1016/j.electacta.2017.01.152
14. Frackowiak, E., Béguin, F., 2001. Carbon materials for the electrochemical storage of energy in capacitors. Carbon 39, 937–950. https://doi.org/10.1016/S0008-6223(00)00183-4
15. González-García, P., 2018. Activated carbon from lignocellulosics precursors: A review of the

synthesis methods, characterization techniques and applications. Renewable and Sustainable Energy Reviews 82, 1393–1414. https://doi.org/10.1016/j.rser.2017.04.117

16. Gu, W., Sevilla, M., Magasinski, A., Fuertes, A.B., Yushin, G., 2013. Sulfur-containing activated carbons with greatly reduced content of bottle neck pores for double-layer capacitors: a case study for pseudocapacitance detection. Energy & Environmental Science 6, 2465. https://doi.org/10.1039/c3ee41182f
17. Guo, D., Shibuya, R., Akiba, C., Saji, S., Kondo, T., Nakamura, J., 2016. Active sites of nitrogen-doped carbon materials for oxygen reduction reaction clarified using model catalysts. Science 351, 361–365. https://doi.org/10.1126/science.aad0832
18. Hou, J., Cao, C., Ma, X., Idrees, F., Xu, B., Hao, X., Lin, W., 2014. From rice bran to high energy density supercapacitors: A new route to control porous structure of 3D carbon. Scientific Reports 4, 1–6. https://doi.org/10.1038/srep07260
19. Huang, S., Guo, H., Li, X., Wang, Z., Gan, L., Wang, J., Xiao, W., 2013. Carbonization and graphitization of pitch applied for anode materials of high power lithium ion batteries. Journal of Solid State Electrochemistry 17, 1401–1408. https://doi.org/10.1007/s10008-013-2003-9
20. Huang, Y., Ma, E., Zhao, G., 2015. Thermal and structure analysis on reaction mechanisms during the preparation of activated carbon fibers by KOH activation from liquefied wood-based fibers. Industrial Crops and Products 69, 447–455. https://doi.org/10.1016/j.indcrop.2015.03.002
21. Hulicova-Jurcakova, D., Seredych, M., Lu, G.Q., Bandosz, T.J., 2009b. Combined effect of nitrogen- and oxygen-containing functional groups of microporous activated carbon on its electrochemical performance in supercapacitors. Advanced Functional Materials 19, 438–447. https://doi.org/10.1002/adfm.200801236
22. Kula, I., Uğurlu, M., Karaoğlu, H., Çelik, A., 2008. Adsorption of Cd(II) ions from aqueous solutions using activated carbon prepared from olive stone by $ZnCl_2$ activation. Bioresource Technology 99, 492–501. https://doi.org/10.1016/j.biortech.2007.01.015
23. Laheaar, A., Delpeux-Ouldriane, S., Lust, E., Beguin, F., 2014. Ammonia Treatment of Activated Carbon Powders for Supercapacitor Electrode Application. Journal of the Electrochemical Society 161, A568–A575. https://doi.org/10.1149/2.051404jes
24. Lee, J., Kim, K.H., Kwon, E.E., 2017. Biochar as a Catalyst. Renewable and Sustainable Energy Reviews 77, 70–79. https://doi.org/10.1016/j.rser.2017.04.002
25. Li, H., Dong, X., da Silva, E.B., de Oliveira, L.M., Chen, Y., Ma, L.Q., 2017. Mechanisms of metal sorption by biochars: Biochar characteristics and modifications. Chemosphere 178, 466–478. https://doi.org/10.1016/j.chemosphere.2017.03.072
26. Lin, Z., Waller, G., Liu, Y., Liu, M., Wong, C.P., 2012. Facile synthesis of nitrogen-doped graphene via pyrolysis of graphene oxide and urea, and its electrocatalytic activity toward the oxygen-reduction reaction. Advanced Energy Materials 2, 884–888. https://doi.org/10.1002/aenm.201200038
27. Liu, Y., Dai, G., Zhu, L., Wang, S., 2018. Green conversion of microalgae into high-performance sponge-like nitrogen-enriched carbon. ChemElectroChem 1–8. https://doi.org/10.1002/celc.201801272
28. Lota, G., Grzyb, B., Machnikowska, H., Machnikowski, J., Frackowiak, E., 2005. Effect of nitrogen in carbon electrode on the supercapacitor performance. Chemical Physics Letters 404, 53–58. https://doi.org/10.1016/j.cplett.2005.01.074
29. Luo, W., Wang, B., Heron, C.G., Allen, M.J., Morre, J., Maier, C.S., Stickle, W.F., Ji, X., 2014.

Pyrolysis of cellulose under ammonia leads to nitrogen-doped nanoporous carbon generated through methane formation. Nano Letters 14, 2225–2229. https://doi.org/10.1021/nl500859p

30. Lv, Y., Zhang, F., Dou, Y., Zhai, Y., Wang, J., Liu, H., Xia, Y., Tu, B., Zhao, D., 2012. A comprehensive study on KOH activation of ordered mesoporous carbons and their supercapacitor application. Journal of Materials Chemistry 22, 93–99. https://doi.org/10.1039/C1JM12742J
31. Oliveira, G., Calisto, V., Santos, S.M., Otero, M., Esteves, V.I., 2018. Paper pulp-based adsorbents for the removal of pharmaceuticals from wastewater: A novel approach towards diversification. Science of the Total Environment 631–632, 1018–1028. https://doi.org/10.1016/j.scitotenv.2018.03.072
32. Paraknowitsch, J.P., Thomas, A., 2013. Doping carbons beyond nitrogen: an overview of advanced heteroatom doped carbons with boron, sulphur and phosphorus for energy applications. Energy & Environmental Science 6, 2839. https://doi.org/10.1039/c3ee41444b
33. Presser, V., Zhang, L., Niu, J.J., McDonough, J., Perez, C., Fong, H., Gogotsi, Y., 2011. Flexible nano-felts of carbide-derived carbon with ultra-high power handling capability. Advanced Energy Materials 1, 423–430. https://doi.org/10.1002/aenm.201100047
34. Ray, A.K., Das, S.K., Mondal, S., Ramachandrarao, P., 2004. Microstructural characterization of bamboo. Journal of Materials Science 39, 1055–1060. https://doi.org/10.1023/B:JMSC.0000012943.27090.8f
35. Salanne, M., Rotenberg, B., Naoi, K., Kaneko, K., Taberna, P.L., Grey, C.P., Dunn, B., Simon, P., 2016. Efficient storage mechanisms for building better supercapacitors. Nature Energy 1, 16070. https://doi.org/10.1038/nenergy.2016.70
36. Shcherban, N., Filonenko, S., Yaremov, P., Dyadyun, V., Bezverkhyy, I., Ilyin, V., 2017. Boron-doped nanoporous carbons as promising materials for supercapacitors and hydrogen storage. Journal of Materials Science 52, 1523–1533. https://doi.org/10.1007/s10853-016-0447-x
37. Shen, W., Fan, W., 2013. Nitrogen-containing porous carbons: synthesis and application. Journal of Materials Chemistry A 1, 999–1013. https://doi.org/10.1039/C2TA00028H
38. Shen, Y., Zhao, P., Shao, Q., Ma, D., Takahashi, F., Yoshikawa, K., 2014. In-situ catalytic conversion of tar using rice husk char-supported nickel-iron catalysts for biomass pyrolysis/gasification. Applied Catalysis B: Environmental 152–153, 140–151. https://doi.org/10.1016/j.apcatb.2014.01.032
39. Sun, L., Tian, C., Fu, Y., Yang, Y., Yin, J., Wang, L., Fu, H., 2014. Nitrogen-doped porous graphitic carbon as an excellent electrode material for advanced supercapacitors. Chemistry - A European Journal 20, 564–574. https://doi.org/10.1002/chem.201303345
40. Tan, Z., Lin, C.S.K., Ji, X., Rainey, T.J., 2017. Returning biochar to fields: A review. Applied Soil Ecology 116, 1–11. https://doi.org/10.1016/j.apsoil.2017.03.017
41. Thommes, M., Kaneko, K., Neimark, A. V., Olivier, J.P., Rodriguez-Reinoso, F., Rouquerol, J., Sing, K.S.W., 2015. Physisorption of gases, with special reference to the evaluation of surface area and pore size distribution (IUPAC Technical Report). Pure and Applied Chemistry 87, 1051–1069. https://doi.org/10.1515/pac-2014-1117
42. Tian, W., Zhang, H., Sun, H., Tadé, M.O., Wang, S., 2018. One-step synthesis of flour-derived functional nanocarbons with hierarchical pores for versatile environmental applications. Chemical Engineering Journal 347, 432–439. https://doi.org/10.1016/j.cej.2018.04.139
43. Vallerot, J.M., Bourrat, X., Mouchon, A., Chollon, G., 2006. Quantitative structural and textural assessment of laminar pyrocarbons through Raman spectroscopy, electron diffraction and few

other techniques. Carbon 44, 1833–1844. https://doi.org/10.1016/j.carbon.2005.12.029
44. Wang, J., Nie, P., Ding, B., Dong, S., Hao, X., Dou, H., Zhang, X., 2017. Biomass derived carbon for energy storage devices. Journal of Materials Chemistry A 5, 2411–2428. https://doi.org/10.1039/C6TA08742F
45. Xu, B., Hou, S., Cao, G., Wu, F., Yang, Y., 2012. Sustainable nitrogen-doped porous carbon with high surface areas prepared from gelatin for supercapacitors. Journal of Materials Chemistry 22, 19088–19093. https://doi.org/10.1039/c2jm32759g
46. Yang, H., Liu, B., Chen, Y., Chen, W., Yang, Q., Chen, H., 2016. Application of biomass pyrolytic polygeneration technology using retort reactors. Bioresource Technology 200, 64–71. https://doi.org/10.1016/j.biortech.2015.09.107
47. Zhang, C., Song, W., Ma, Q., Xie, L., Zhang, X., Guo, H., 2016. Enhancement of $CO_2$ Capture on Biomass-Based Carbon from Black Locust by KOH Activation and Ammonia Modification. Energy and Fuels 30, 4181–4190. https://doi.org/10.1021/acs.energyfuels.5b02764
48. Zhao, H.B., Wang, W.D., Lu, Q.F., Lin, T.T., Lin, Q., Yang, H., 2015. Preparation and application of porous nitrogen-doped graphene obtained by co-pyrolysis of lignosulfonate and graphene oxide. Bioresource Technology 176, 106–111. https://doi.org/10.1016/j.biortech.2014.11.035
49. Zhu, H.M., Yan, J.H., Jiang, X.G., Lai, Y.E., Cen, K.F., 2008. Study on pyrolysis of typical medical waste materials by using TG-FTIR analysis. Journal of Hazardous Materials 153, 670–676. https://doi.org/10.1016/j.jhazmat.2007.09.011

**Figure Caption**

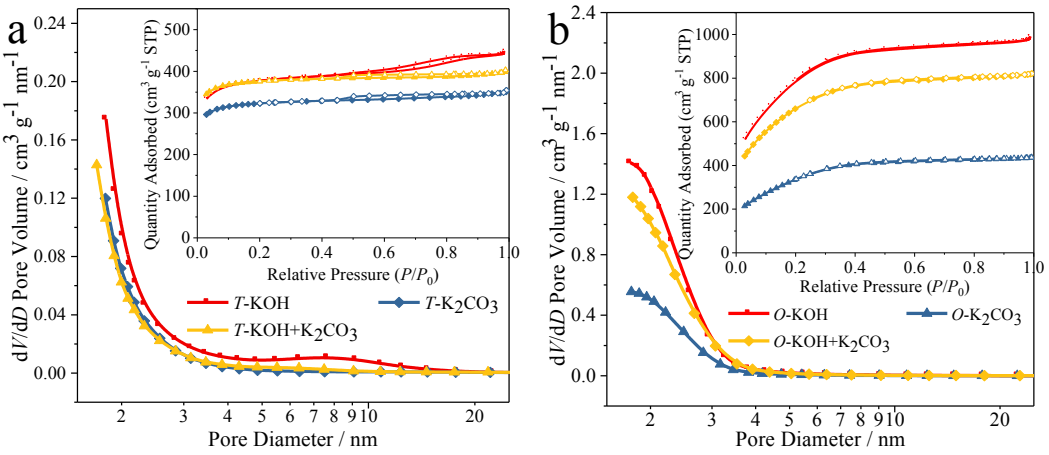


**Figure 1.** Adsorption pore size distributions and $N_2$ sorption isotherms (insets) of the ACs prepared via the (a) two-step and (b) one-step methods.

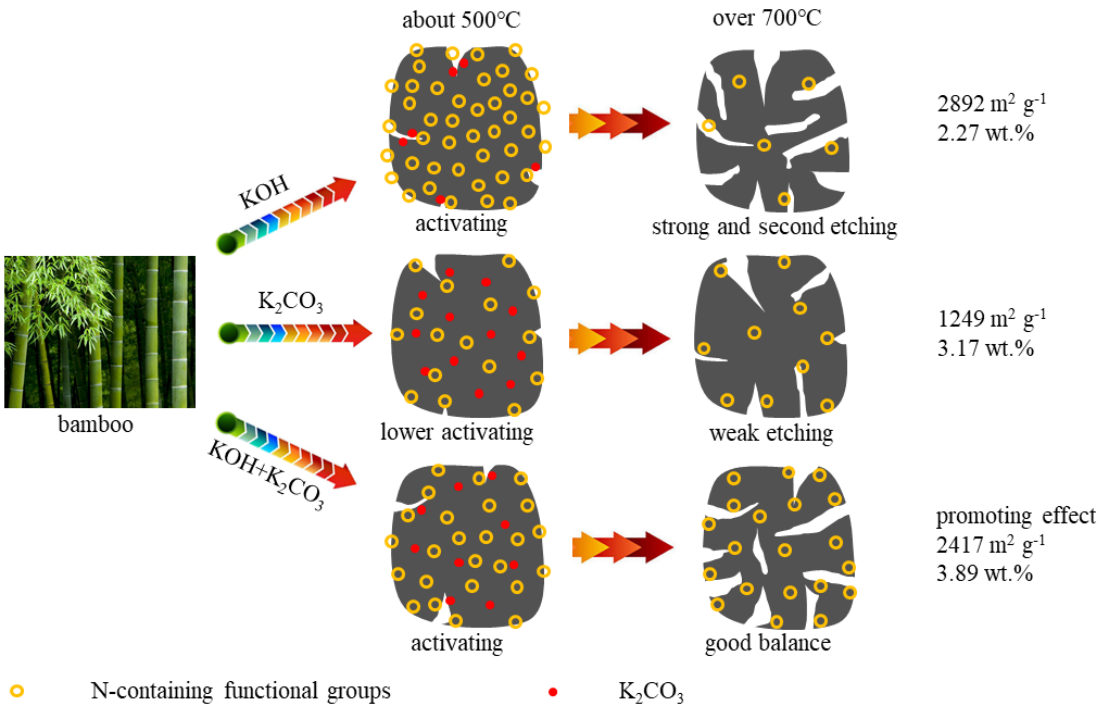


**Figure 2.** Proposed reaction process for the one-step method under $NH_3$ atmosphere.

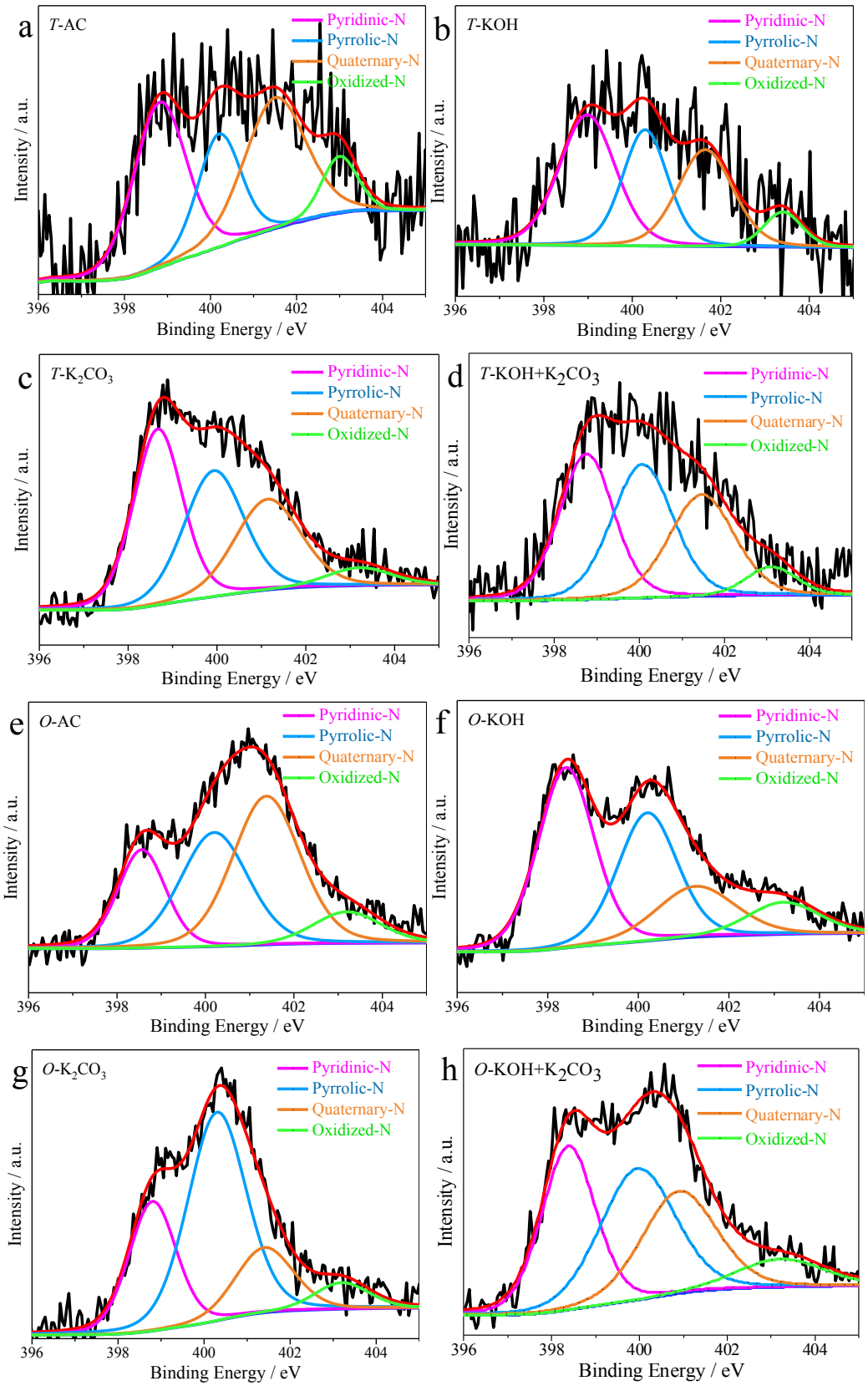


**Figure 3.** N 1*s* spectra of ACs prepared via (a), (b), (c), and (d) the two-step method and (e), (f), (g), and (h) the one-step method.

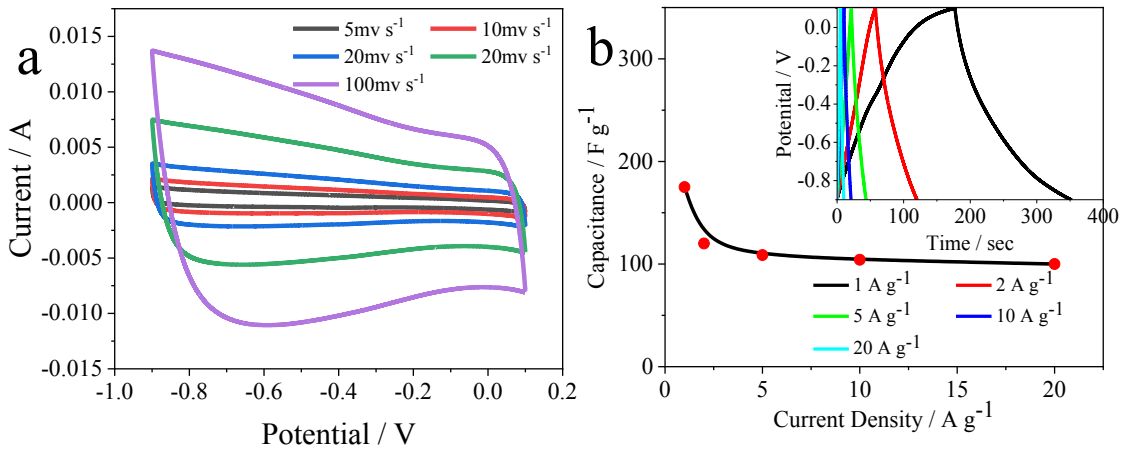


**Figure 4.** (a) CV curves of *O*-KOH+$K_2CO_3$ at scan rates from 5 to 100 mV $s^{-1}$; (b) Specific capacitance of *O*-KOH+$K_2CO_3$ at current densities from 1 to 20 A $g^{-1}$ (inset shows GCD curves at different densities).

**Table 1** Pore characteristics of ACs derived from pyrolysis of bamboo waste

| Sample | $S_{BET}$ ($m^2 g^{-1}$) | $S_{mic}$ ($m^2 g^{-1}$) | $S_{mic}/S_{BET}$ (%) | $V_{total}$ ($cm^3 g^{-1}$) | $D$ (nm) |
|---|---|---|---|---|---|
| *T*-AC | 245 | - | - | 0.081 | - |
| *T*-KOH | 1276 | 996 | 78 | 0.756 | 2.369 |
| *T*-$K_2CO_3$ | 1268 | 1095 | 86 | 0.623 | 1.965 |
| *T*-KOH+$K_2CO_3$ | 1123 | 925 | 82 | 0.548 | 2.020 |
| *O*-AC | 521 | - | - | 0.075 | - |
| *O*-KOH | 2892 | 63 | 2 | 1.533 | 2.120 |
| *O*-$K_2CO_3$ | 1249 | 113 | 9 | 0.676 | 2.164 |
| *O*-KOH+$K_2CO_3$ | 2417 | 184 | 8 | 1.270 | 2.102 |

**Table 2** N-doping concentrations, types, and proportions in the ACs from the ultimate and XPS analyses

| Sample | $N_{UA}$[a]/wt% | $N_{XPS}$/at% | Pyridinic-N/% | Pyrrolic-N/% | Quaternary-N/% | Oxidized-N/% |
|---|---|---|---|---|---|---|
| *T*-AC | 1.68 | 0.91 | 36.66 | 20.60 | 34.17 | 8.57 |
| *T*-KOH | 1.15 | 0.50 | 38.16 | 27.15 | 27.82 | 6.87 |
| *T*-$K_2CO_3$ | 2.64 | 2.10 | 37.01 | 32.30 | 25.76 | 4.94 |
| *T*-KOH+$K_2CO_3$ | 1.08 | 0.78 | 32.71 | 33.91 | 27.38 | 6.00 |
| *O*-AC | 2.99 | 2.87 | 19.09 | 31.37 | 40.88 | 8.65 |
| *O*-KOH | 2.27 | 2.96 | 42.08 | 31.66 | 16.69 | 9.57 |
| *O*-$K_2CO_3$ | 3.17 | 2.76 | 26.08 | 51.64 | 16.15 | 6.14 |
| *O*-KOH+$K_2CO_3$ | 3.89 | 3.82 | 30.75 | 34.22 | 26.56 | 8.47 |

[a]ultimate analysis, dry basis.